Sol−Gel-Derived Ceria Nanoarchitectures: Synthesis, Characterization, and Electrical Properties

Christel Laberty-Robert,*[,†,‡] Jeffrey W. Long,[†] Erik M. Lucas,[†] Katherine A. Pettigrew,[†,§] Rhonda M. Stroud,[§] Michael S. Doescher,[†] and Debra R. Rolison*[,†]

Naval Research Laboratory, Surface Chemistry (Code 6170) and Materials and Sensors (Code 6360) Branches, 4555 Overlook Avenue, SW, Washington, D.C. 20375, and Centre Inter-universitaire de Recherche et d'Ingénierie des MATériaux, CNRS-UMR 5085, Université Paul Sabatier, 118 route de Narbonne, 31062 Toulouse Cedex 04, France

Received June 26, 2005. Revised Manuscript Received October 14, 2005

Nanocrystalline ceria is under study to improve performance in high-temperature catalysis and fuel cells. We synthesize porous ceria monolithic nanoarchitectures by reacting Ce(III) salts and epoxide-based proton scavengers. Varying the means of pore-fluid removal yields nanoarchitectures with different pore−solid structures: aerogels, ambigels, and xerogels. The dried ceria gels are initially X-ray amorphous, high-surface-area materials, with the aerogel exhibiting 225 m^2 g^{-1}. Calcination produces nanocrystalline materials that, although moderately densified, still retain the desirable characteristics of high surface area, through-connected porosity in the mesopore size range and nanoscale particle sizes (∼10 nm). The electrical properties of calcined ceria ambigels are evaluated from 300 to 600 °C and compared to those of commercially available nanoscale CeO_2. The pressed pellets of both ceria samples exhibit comparable surface areas and void volumes. The conductivity of the ceria ambigel is 5 times greater than the commercial sample and both materials exhibit an increase in conductivity in argon relative to oxygen at 600 °C, suggesting an electronic contribution to conductivity at low oxygen partial pressures. The ceria ambigel nanoarchitecture responds to changes in atmosphere at 600 °C faster than does the nanocrystalline, non-networked ceria. We attribute the higher relative conductivity of CeO_2 ambigels to the bonded pathways inherent to the bicontinuous pore−solid networks of these nanoarchitectures.

Introduction

Cerium oxides are important catalysts for reforming hydrocarbons, the partial oxidation of methane in solid-oxide fuel cells (SOFC),[1−3] and for direct hydrogen production via the water-gas-shift reaction.[4−6] The performance of ceria-based materials in these applications is largely due to the ease in generating Ce(III) from Ce(IV).[7] Pure CeO_2 is reduced at high temperature and low oxygen partial pressure, resulting in oxygen deficiency and partial electronic conductivity, which is advantageous for the water-gas-shift reaction and charge transport in SOFC electrode structures. These innate properties of ceria-based materials may be further amplified by producing ceria in nanostructured forms.

Aerogels and ambigels are classes of sol−gel-derived materials that are composed of bicontinuous networks of solid and pore.[8−11] The inherent characteristics of such nanoarchitectures are highly beneficial for many applications, particularly those that are rate critical.[12] For example, the through-connected pore network of the aerogel accommodates the rapid diffusional transport of gas-phase reactants and products.[13,14] The combination of high surface area and facile gas flux through the structure makes aerogels particularly attractive for heterogeneous catalysis.[11,15,16] Electrically conductive aerogels, with compositions such as carbon and transition metal oxides, have also been shown to exhibit superior performance for a range of electrochemical applications.[10,12,17,18] Aerogel-based electrodes benefit not only from high surface area and porosity but also from the bonded solid network that comprises the aerogel skeleton and promotes long-range electronic and electrical conduction. Recently, we demonstrated that the contiguous extended pathways available within an unbroken MnO_2 ambigel structure are crucial for long-range, surface-restricted ionic conduction.[19] This

---

* To whom correspondence should be addressed. E-mail: laberty@ccs.nrl.navy.mil; rolison@nrl.navy.mil.

[†] Code 6170, Naval Research Laboratory.

[‡] Université Paul Sabatier.

[§] Code 6360, Naval Research Laboratory.

(1) Steele, B. C. H. *J. Power Sources* **1994**, *49*, 1−14.
(2) Steele, B. C. H. *Solid State Ionics* **2000**, *129*, 95−110.
(3) Park, S. D.; Vohs, J. M.; Gorte R. J. *Nature (London)* **2000**, *404*, 265−267.
(4) He, H.; Dai, H.; Au, C. T. *Catal. Today* **2004**, *90*, 245−254.
(5) Jacobs, G.; Khalid, S.; Patterson, P. M.; Sparks, D. E.; Davis, B. H. *Appl. Catal., A* **2004**, *268*, 255−256.
(6) Trovalli, A. *Catal. Rev.-Sci. Eng.* **1996**, *48*, 439−520.
(7) Tschöpe, A. *J. Electroceram.* **2005**, *14*, 5−23.
(8) Fricke, J.; Emmerling, A. *J. Sol-Gel Sci. Technol.* **1998**, *13*, 299−303.
(9) Hüsing, N.; Schubert, U. *Angew. Chem., Int. Ed.* **1998**, *37*, 23−45.
(10) Rolison, D. R.; Dunn, B. *J. Mater. Chem.* **2001**, *11*, 963−980.
(11) Pierre, A. C.; Pajonk, G. M. *Chem. Rev.* **2002**, *102*, 4243−4265.
(12) Rolison, D. R. *Science* **2003**, *299*, 1698−1701.
(13) Leventis, N.; Elder, I. A.; Rolison, D. R.; Anderson, M. L.; Merzbacher, C. I. *Chem. Mater.* **1999**, *11*, 2837−2845.
(14) Wallace, J. M.; Rice, J. K.; Pietron, J. J.; Stroud, R. M.; Long, J. W.; Rolison, D. R. *Nano Lett.* **2003**, *3*, 1463−1467.
(15) Pajonk, G. M. *Appl. Catal.* **1991**, *72*, 217−266.
(16) Schneider, M.; Baiker, A. *Catal. Today* **1997**, *35*, 339−365.
(17) Owens, B. B.; Passerini, S.; Smyrl, W. H. *Electrochim. Acta* **1999**, *45*, 215−224.
(18) Frackowiak, E.; Beguin, F. *Carbon* **2001**, *39*, 937−950.

10.1021/cm051385t CCC: $33.50

same set of characteristics would be highly desirable in a cerium oxide composition.

The synthesis of cerium oxides with high specific surface areas has been achieved via hydrothermal synthesis,[20] spray pyrolysis,[21] surfactant-templated synthesis,[22] coprecipitation,[23] autoignition,[24] glycine-nitrate combustion,[25] and hydrazine reduction.[26] Materials with specific surface areas ranging from 100 to 200 $m^2\ g^{-1}$ are obtained, but these oxides exhibit broad pore-size distributions, or in some cases networks of small, one-dimensional pores. There are relatively few studies focused on the preparation and properties of mesoporous cerium oxide. In 1993, Hoang-Van et al. reported the preparation of mesoporous ceria by sol−gel methods and obtained aerogels by supercritically drying alcogels derived from Ce-acetylacetone.[27] The specific surface areas of the amorphous compounds varied from 65 to 100 $m^2\ g^{-1}$. Recently, ceria aerogels with high surface area and high porosity were prepared from gels obtained from the hydrolysis of Ce-methoxyethanol in excess methoxyethanol.[28] The unheated aerogel was reported to be crystalline and exhibited a specific surface area of 349 $m^2\ g^{-1}$ with an average pore diameter of ~21.3 nm and porosity of 90%. However, no electrical measurements of the porous ceria aerogels were reported in these papers. If these nanoarchitectures are to be explored for SOFC application, it will be critical to understand their fundamental electrical properties, especially at relevant temperatures, which are typically >500 °C.

In this report, we describe the synthesis of monolithic ceria gels, which are ultimately processed to dry gels (aerogels, ambigels, and xerogels), each of which exhibits a distinct pore−solid nanoarchitecture. Ceria gels are achieved via the reaction of Ce(III) salts and propylene oxide,[29] in a modification of an innovative synthetic method recently reported by Gash and co-workers for the preparation of transition-metal-oxide aerogels.[30−32] The electrical properties of these porous nanoarchitectures are reported and compared to a commercially available, high-surface-area nanocrystalline cerium oxide. Our investigations demonstrate that the relationship of the ionic and electronic conductivities of porous ceria nanoarchitectures differ from those in bulk ceria and agglomerated nanocrystalline ceria.

Experimental Procedures

Synthesis of Ceria Gels. The synthesis of cerium oxide gels was achieved using a minor modification of the protocol published by Gash et al. for the synthesis of iron and chromium oxides.[30−32] The epoxide used in this work is propylene oxide (Aldrich, 99%) [**Safety Note**: this epoxide is carcinogenic] and the metal salt is $Ce(III)Cl_3 \cdot 6H_2O$ (Aldrich, 99.9%). Attempts to synthesize ceria gels by the Gash protocol using as-received propylene oxide usually resulted in precipitates, rather than monolithic gels. For this particular synthesis, we determined that it was necessary to first purify the propylene oxide by passing it through a packed column of activated alumina (Alfa Aesar) just prior to introducing the epoxide into the reaction mixture. This purification step likely removes hydrolyzed and/or oligomerized propylene oxide, which result from its high reactivity. Less reactive epoxides such as epichlorohydrin and epibromohydrin did not produce stable ceria gels.

In a typical preparation, the purified propylene oxide (16 mmol) is added in one aliquot to a stirring solution of $CeCl_3 \cdot 6H_2O$ (1.6 mmol) in 2.77 mL of anhydrous methanol (Mallinckrodt). After the addition of propylene oxide, the solution was milky white and over 20 min changed to an intense brown. The sol is poured into one of several polypropylene molds, where gelation typically occurs within ~1 h. The wet gel is covered and allowed to age overnight under ambient conditions. Gels were also obtained at a molar propylene oxide:Ce(III) ratio of 18:1, but all the samples described in this work were synthesized at a 10:1 molar ratio.

Processing of CeO_x Gels. The aged gels are rinsed with several aliquots of anhydrous 2-propanol (Mallinckrodt) to remove soluble byproducts, followed by a series of rinses in acetone (Fisher, used as-received). Rinsing with methanol or ethanol led to dissolution of the gels. The acetone-filled gels are then processed to form xerogels, ambigels, and aerogels by varying the rinsing and drying procedures.

Xerogels. Excess acetone was decanted and the gels were dried in a chamber at 60 °C under flowing nitrogen over 2 days to form xerogels.

Ambigels. Acetone is replaced daily with fresh cyclohexane over 4−5 days. The wet gels are then dried at 60 °C under flowing nitrogen over 2 days to form ambigels.

Aerogels. The acetone-filled gels are transferred under acetone into a critical-point dryer (Polaron Range, Quorum Technologies, New Haven, East Sussex, UK) maintained at 10 °C; the autoclave is then filled with liquid CO_2. After a series of exchanges with liquid CO_2 over 6 h, the temperature within the autoclave is increased beyond the critical point of CO_2 ($T_c = 31$ °C; $P_c = 7.4$ MPa). Supercritical CO_2 is slowly vented from the autoclave, resulting in dry cerium oxide (CeO_x) aerogels that retain the dimensions of the wet gel.

The as-synthesized samples (aerogels, ambigels, and xerogels) are light brown, suggesting the presence of residual organic byproducts and cerium 4+. The as-dried CeO_x gels are calcined in static air at either 300 or 600 °C at a heating rate of 5 °C min^{-1} and held at the designated temperature for 2 h. The color of the calcined oxides changes from light brown to pale yellow, indicating the removal of organic byproducts.

Characterization. Simultaneous thermogravimetric analysis (TGA) and differential scanning calorimetry (DSC) were performed (Rheometrics STA1500) under either flowing oxygen or argon at a heating rate of 2 °C min^{-1}. Infrared spectra were recorded from

---

(19) Doescher, M. S.; Pietron, J. J.; Dening, B. M.; Long, J. W.; Rolison, D. R. *Anal. Chem.* **2005**, *77*, 7924−7932.

(20) Hirano, M.; Kato, E. *J. Am. Ceram. Soc.* **1996**, *79*, 777−780.

(21) Gesser, H. D.; Goswami, P. C. *Chem. Rev.* **1989**, *89*, 765−788.

(22) Masui, T.; Fujiwara, K.; Machida, K.; Adachi, G.; Sakata, T.; Mori, H. *Chem. Mater.* **1997**, *9*, 2197−2204.

(23) Pijolat, M.; Viricelle, J. P.; Sosutelle, M. *Stud. Surf. Sci. Catal.* **1997**, *91*, 885−891.

(24) Basu, S.; Sujatha Devi, P.; Maiti, H. S. *J. Mater. Res.* **2004**, *19*, 3162−3171.

(25) Purohit, R. D.; Sharma, D.; Pillai K. T.; Tyagi, A. K. *Mater. Res. Bull.* **2001**, *36*, 2711−2716.

(26) Nakane, S.; Tachi, T.; Yoshinaka, M.; Hirota, K.; Yamaguchi, O. *J. Am. Ceram. Soc.* **1997**, *80*, 3221−3227.

(27) Hoang-Van, C.; Harivololona, R.; Pommier, B. *Stud. Surf. Sci. Catal.* **1995**, *91*, 435−443.

(28) Thundathil, M. A.; Lai, W.; Noailles, L.; Dunn, B. S.; Haile, S. M. *J. Am. Ceram. Soc.* **2004**, *87*, 1442−1445.

(29) Lucas, E. M.; Long, J. W.; Rolison, D. R. In *Abstracts of the 7th International Symposium on Aerogels*, Alexandria, VA, 2−5 November 2003; SA, Inc.: Arlington, VA, 2003.

(30) Gash, A. E.; Tillotson, T. M.; Satcher, J. H.; Poco, J. F.; Hrubesh, L. W.; Simpson, R. L. *Chem. Mater.* **2001**, *13*, 999−1007.

(31) Gash, A. E.; Tillotson, T. M.; Satcher, J. H.; Hrubesh, L. W.; Simpson, R. L. *J. Non-Cryst. Solids* **2001**, *285*, 22−28.

(32) Gash, A. E.; Satcher, J. H.; Simpson, R. L. *Chem. Mater.* **2003**, *15*, 3268−3275.

4000 to 400 cm^{-1} (Nicolet Magna-IR, Spectrometer 750). Powder X-ray diffraction data were collected at room temperature (Bruker D8 Advance X-ray diffractometer) with Cu Kα radiation in the Bragg−Brentano geometry. Grain/particle size measurements were made by applying the Scherrer equation to the full-width at half-maximum (fwhm) of the ⟨111⟩, ⟨200⟩, ⟨220⟩, ⟨311⟩, ⟨222⟩, and ⟨400⟩ peaks after accounting for instrumental broadening using silicon as reference.

Transmission electron microscopy was used to characterize the morphologies of the heat-treated materials and to confirm particle size and crystal structure. Samples were prepared by dry-grinding the as-prepared powders and then brushing the dust onto holey-carbon film supports. The data were obtained using a JEOL 2010F TEM equipped with a Gatan CCD camera. To verify the nature of the particle agglomeration or interconnectivity of the 600 °C-calcined ceria ambigel and commercial powders, these samples were examined by scanning electron microscopy (Leo Supra 55); the powders were brushed onto carbon tape for analysis and analyzed without overcoating with conductive gold or carbon. Specific surface area and pore-size distribution were derived from nitrogen adsorption/desorption isotherms obtained at 77 K (Micromeritics ASAP2010 surface area analyzer); samples were degassed overnight at 200 °C. Pore-size distributions were calculated from adsorption isotherm data using Micromeritics DTFPlus software (Halsey Thickness model, cylindrical pores).

Impedance measurements (Solartron SI-1260 Impedance/gain-phase analyzer) from 20 MHz to 1 Hz with a sampling interval of 10 per decade were performed on 600 °C-calcined ceria powders that were pressed into pellets (diameter 13 mm × 1.02 mm) using a pressure of 5000 lbs for 2 min in an IR pellet press. For comparison, pellets were also prepared from commercial $CeO_2 \cdot xH_2O$ (Alfa Aesar) that had been calcined in static air at 600 °C for 2 h. Surface area and pore volume measurements were made on both the powder and pelletized forms to determine the effect of pressing on the pore structure of the powders. The pellets (commercial or ambigel) exhibit ~85% of the theoretical density of CeO_2 (7.216 g cm^{-3}). The ceria pellets were held in a conductivity cell comprising two stainless-steel plates using either platinum or gold foils as the electrode contacts. Sample cells were placed in a quartz tube (32 mm in diameter) furnace and heated under a positive pressure of O_2 or argon gas. To determine the activation energy of conduction, measurements were made in 50 °C steps between 350 and 600 °C; the furnace was ramped at a rate of 10 °C min^{-1} and allowed to equilibrate at each temperature stage for 1 h before each measurement. The impedance spectra were recorded in either oxygen or argon flowing at 14 cm min^{-1}.

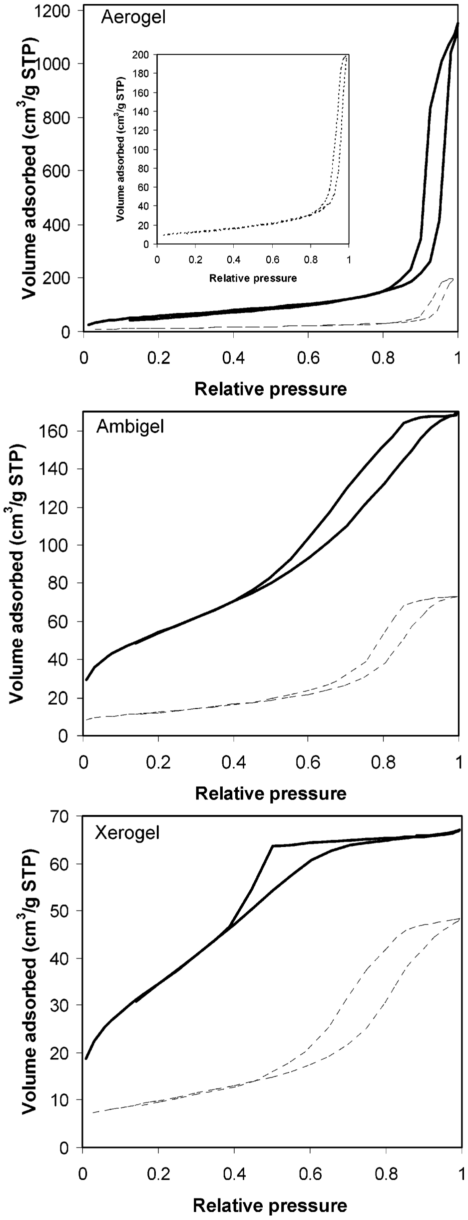

Figure 1. Nitrogen adsorption/desorption isotherms for various CeOx nanoarchitectures (aerogel, ambigel, and xerogel): (−) as-prepared samples; (- - -) samples calcined in air at 600 °C; aerogel inset: expanded *y*-axis for the 600 °C-calcined material.

Results and Discussion

Characterization of As-Prepared CeO$_x$. The microstructure of as-synthesized CeO$_x$ aerogel and ambigel is highly porous and uniform, as evidenced by the results of the N_2 adsorption studies. The adsorption/desorption isotherms for the three pore−solid nanoarchitectures (xerogel, aerogel, and ambigel), as-synthesized and after calcination at 600 °C are shown in Figure 1. All nanoarchitectures have isotherms consistent with mesoporosity, and all exhibit a Type 4 isotherm.[33]

The data derived from the BET and BJH fits are reported in Table 1. The as-prepared CeO$_x$ aerogel has a large specific surface area of 225 m^2 g^{-1} and large average pore size (around 50 nm). The as-prepared ambigel also presents a high specific surface area of 200 m^2 g^{-1}. However, compared to the pore distribution in aerogels (Figure 2), the macropores are lost in the ambigel and the pore volume is distributed with a peak centered at 15 nm. The as-prepared xerogel has a moderate specific surface area (85 m^2 g^{-1}) and pores restricted to <20 nm. All forms of the as-prepared CeO$_x$ gels were amorphous as determined by powder X-ray diffraction (data shown in Supporting Information).

As most of the applications of ceria-based materials require high-temperature operation (300−900 °C), we examined the effects of various thermal treatments on these porous CeO$_x$ nanoarchitectures. Prior to thermal treatments, the as-prepared gels were first examined using simultaneous thermal analysis (TGA/DSC) to determine the temperatures necessary to dehydrate and crystallize the nanoscale CeO$_x$. The as-prepared CeO$_x$ aerogels exhibit thermogravimetric transitions

---

(33) Webb, P. A.; Orr, C. *Analytical Methods in Fine Particle Technology*; Micromeritics Instrument Corp.: Norcross, GA, 1997.

Table 1. Physical Properties of As-Prepared Ceria (Ambigels, Xerogels, and Aerogels) and Commercial Ceria as a Function of Heat Treatment and Drying Steps

ceria architecture	treatment[a]	BET surface area ($m^2 g^{-1}$)[b]	cumulative pore volume[c] $cm^3 g^{-1}$	average pore diameter[c] (nm)	particle size XRD[d] (nm)	particle size TEM (nm)
aerogels	as-prepared	225	1.78	24		
300-aerogels	300 °C in air	87	0.33	9		
600-aerogels	600 °C in air	70	0.47	12	11	5−15
600-aerogels	pelletized	51	0.13	10		
ambigels	as-prepared	200	0.21	7		
300-ambigels	300 °C in air	197	0.26	5		
600-ambigels	600 °C in air	45	0.11	10	12	7−13
600-ambigels	pelletized	41	0.09	9		
xerogels	as-prepared	75	0.32	18		
300-xerogels	300 °C in air	55	0.22	9		
600-xerogels	600 °C in air	35	0.07	8	13	8−20
600-xerogels	pelletized	37	0.08	8		
600-commercial	600 °C in air	52	0.17	13		
600-commercial	pelletized	39	0.12	12		

[a] Samples are heat-treated in static air at the desired temperature for 2 h, with a heating rate of 2 °C min^{-1} to reach temperature. [b] Multipoint BET method, the accuracy is ±5%; three separate synthetic batches were prepared and the values differ by ±10%. [c] BJH method using the adsorption isotherm, representing the volume in pores between 1.7 and 300 nm. [d] Scherrer analysis of the ⟨111⟩, ⟨200⟩, ⟨220⟩, ⟨311⟩, ⟨222⟩, and ⟨400⟩ diffraction peaks.

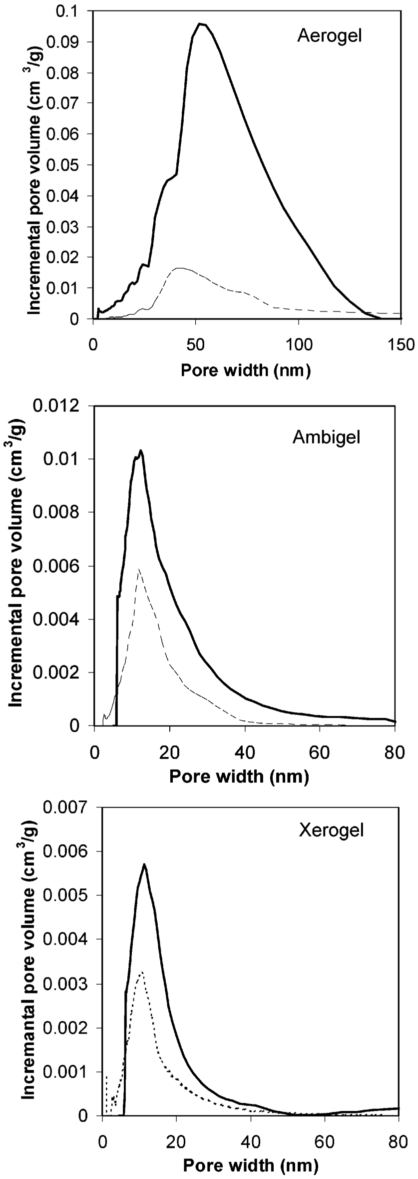

Figure 2. Pore-size distribution plots derived from N_2 adsorption isotherms of uncalcined and calcined CeOx nanoarchitectures: (−) as-prepared samples; (- - -) nanoarchitectures calcined in air at 600 °C.

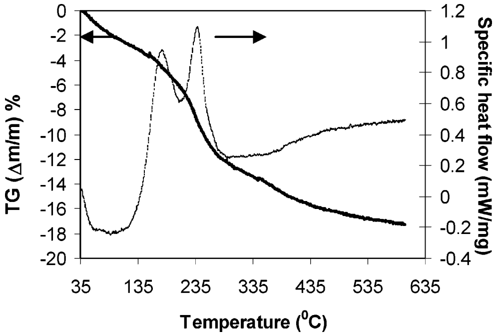

Figure 3. Thermogravimetric and differential calorimetric analysis of an as-synthesized CeO_2 aerogel under O_2 at a heating rate of 5 °C min^{-1}.

due to the loss of physisorbed water and structural water, as well as decomposition/volatilization of organic byproducts of the initial synthesis (Figure 3). The loss of physisorbed water, in the range of 35−135 °C, is confirmed in simultaneous DSC analyses, where an endotherm is observed. Upon further heating in air, we observe two sharp exothermic peaks, the first at 180 °C and the second at 260 °C, both of which occur with corresponding weight loss. We attribute these exothermic events to the loss of hydroxyl groups from the CeO_x gel surface, oxidation of residual organic byproducts, and crystallization of the nanoscale ceria.

Upon heating to 300 °C, the as-prepared CeO_x turns from brown to yellow. The loss of the brown color is indicative of the thermal degradation of organic byproducts, while the final yellow color of the sample indicates transformation from cerium oxyhydroxide/oxide to nonstoichiometric CeO_2. Ex situ FTIR spectroscopy was used to assess the presence of residual organics and hydroxyl ions/water in the CeO_x aerogels subjected to various heat treatments (spectra shown in Supporting Information). X-ray photoelectron spectroscopic analysis of as-prepared versus 600 °C-calcined samples also verifies the loss of organochlorine species after calcination (see Supporting Information). These measurements confirm that residual organics and physisorbed water are eliminated after heating the as-prepared materials in air for 2 h at 600 °C. The C−H bending mode at ∼1300 cm^{-1} is absent after calcination at 600 °C; however, some carbon (in the form of oxygenated species, probably carbonate) is still present, due to the rapid adsorption of atmospheric contaminants onto the ceria aerogel. In the present work, the calcination temperature is limited to ≤600 °C.

Thermal Processing and Characterization of CeO_2 Aerogels and Ambigels. Calcination of the ceria gels at 300 and 600 °C crystallizes the ceria domains and strongly affects the porosity and surface areas for these pore−solid nanoarchitectures (see Table 1). Heat treatment reduces the void volume, changes the pore-size distribution (PSD), and increases the average grain size (Table 1). However, the overall microstructure of the aerogel and the ambigel retains the characteristics of nanoscale networked solid and interconnected porosity in the mesopore size range. After calcination at 600 °C, the specific surface area decreases from 225 $m^2\ g^{-1}$ for the as-synthesized aerogel to 70 $m^2\ g^{-1}$ and from 200 to 45 $m^2\ g^{-1}$ for the ambigel. The average grain or particle size increases from a value not detectable by X-ray diffraction (typically <5 nm) to almost 11 nm for the aerogel and 12 nm for the ambigel.

The reduction of void volume in the aerogel and ambigel after calcination at 600 °C is shown by the sharp decrease in the cumulative pore volume from 1.78 to 0.47 $cm^3\ g^{-1}$ and 0.21 to 0.11 $cm^3\ g^{-1}$, respectively. As seen in the PSD plot (Figure 2), this densification in the aerogel nanoarchitecture is due to the collapse of pores in the entire size range (1−120 nm) and the volume-weighted peak shifts from 60 to 40 nm. The densification in the ambigel form arises mostly from collapse of pores in the 20−40-nm size range with no significant change in the volume-weighted peak. Although heat treatment affects the physical nature of the ambigel and aerogel nanoarchitectures, they remain more attractive than conventional xerogel samples of similar composition, which exhibit much lower surface area and small mesopores (Table 1). The advantage of the ambigel form compared to the aerogel is that ambient-pressure drying is used, which may be a preferable approach for large-scale production, whereas aerogels require supercritical-fluid processing.

Transmission Electron Microscopy and X-ray Diffraction. Both electron diffraction and X-ray powder diffraction were used to measure the particle size and identify the crystalline structure. The X-ray diffraction pattern of as-prepared ceria aerogel contained broad peaks, difficult to attribute to any known phases of cerium oxide (data shown in Supporting Information). Upon heating at 300 °C, the diffraction peaks sharpen with better signal-to-noise, indicating the formation of nanocrystalline CeO_2 (Figure 4). The X-ray powder diffraction patterns of the aerogels, ambigels, and xerogels calcined at 600 °C are consistent with the known cubic phase for CeO_2. These data index as cerium(IV) oxide with the cubic fluorite structure, in good agreement with literature values.[34] In addition, the degree of crystallinity of the aerogel calcined at 600 °C appears to be greater than that of the 600 °C-calcined ambigel (Figure 4b) because the intensity ratio between the (*hkl*) peaks relative to the (111) peak is greater for the aerogel.

The heat treatment at 600 °C induced growth of the networked particles in all the samples, which can be seen by TEM (Figures 5 and 6). In general, the microstructure of these nanoarchitectures appears to consist of randomly oriented, networked nanocrystalline particles. The calcined aerogels have particle sizes of 5−15 nm, which is comparable to calcined ambigel (7−13 nm). The xerogels have larger particles (8−20 nm) than either the aerogel or ambigel ceria. The high-resolution TEM, HRTEM, of the xerogel ceria shows a more crowded network of particles. The HRTEM of the aerogel shows well-defined crystallites with strong faceting and well-defined edges (Figure 6); most particles exhibit lattice fringes. These microstructural characteristics are particularly attractive for catalytic performance.[35] Similar high-resolution images are observed for the ambigel. Analysis of the lattice fringes yields *d* spacings that match those of nanocrystalline ceria from the literature[34] and the JCPDS crystal database.

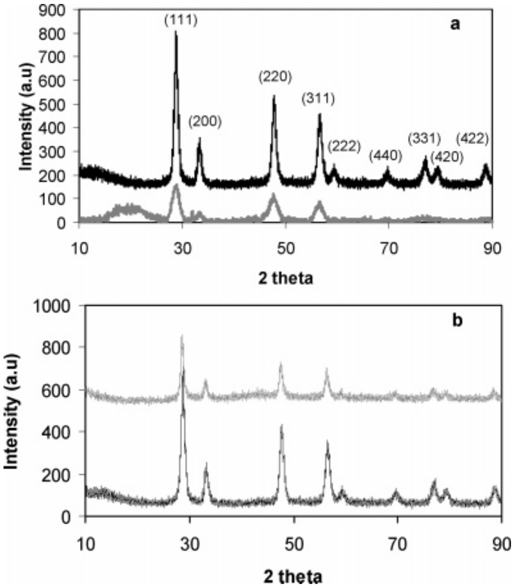

Figure 4. Powder X-ray diffraction patterns (background-corrected) of CeO_2 nanoarchitectures: (a) aerogel calcined at 300 °C (gray) and 600 °C (black); (b) contrasting a 600 °C-calcined aerogel (black) with a 600 °C-calcined ambigel (gray).

Electrical Properties of CeO_2 Ambigel. The CeO_2 nanoarchitectures prepared in this study exhibit the desirable physical attributes of high specific surface area, an interconnected porous network, and bonded networks of nanoscale CeO_2 crystallites—qualities that should be highly beneficial for SOFC electrodes. Therefore, it is necessary to characterize the electrical properties of such nanoarchitectures; however, previous reports on related ceria nanoarchitectures did not include electrical characterization. It is especially important to determine whether the electrical properties depend on the nature of the pore−solid nanoarchitecture. We examined the impedance behavior of CeO_2 nanocrystalline samples in the form of pressed pellets derived from the respective powder forms of commercially available ceria, ceria ambigel, and ceria aerogel after calcination of all materials. The electrical response of ceria aerogel is comparable to that of the ambigel; below, we focus on the comparison of ambigel and nanocrystalline ceria.

---

(34) Leoni, M.; Di Maggio, R.; Polizzi, S.; Scardi, P. *J. Am. Ceram. Soc*. **2004**, *87*, 1133−1140.

(35) Sun, N.; Klabunde, K. J. *J. Catal*. **1999**, *185*, 506−512.

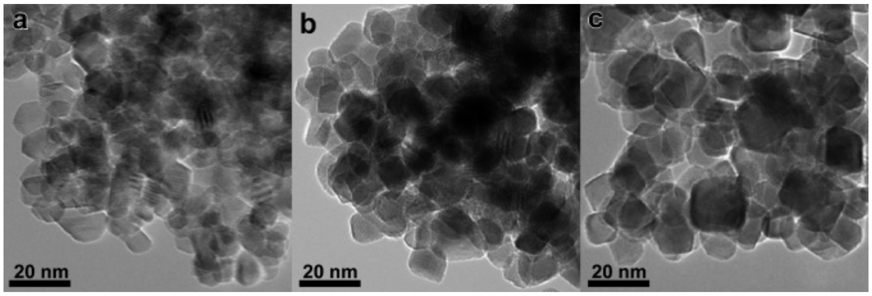

Figure 5. Transmission electron micrographs of ceria nanoarchitectures calcined at 600 °C: (a) aerogel; (b) ambigel; and (c) xerogel.

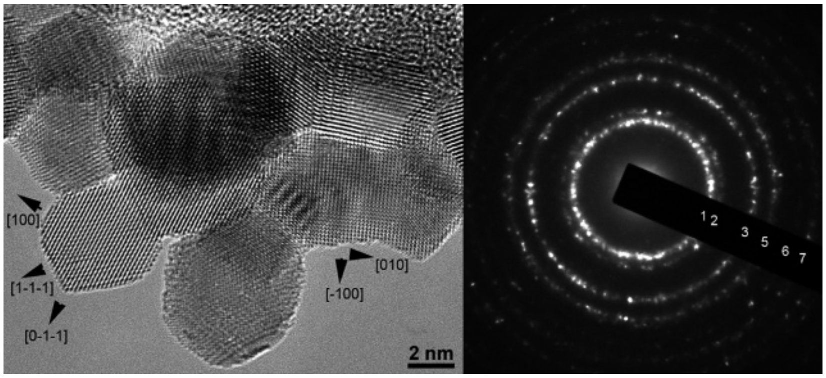

Figure 6. High-resolution transmission electron micrograph (left) and electron diffraction pattern of CeO_2 aerogel calcined at 600 °C (1, 0.312 nm (111); 2, 0.273 nm (200); 3, 0.189 nm (220); 4, 0.161 nm (311); 5, 0.135 nm (400); 6, 0.123 nm (331); 7, 0.110 nm (422)).

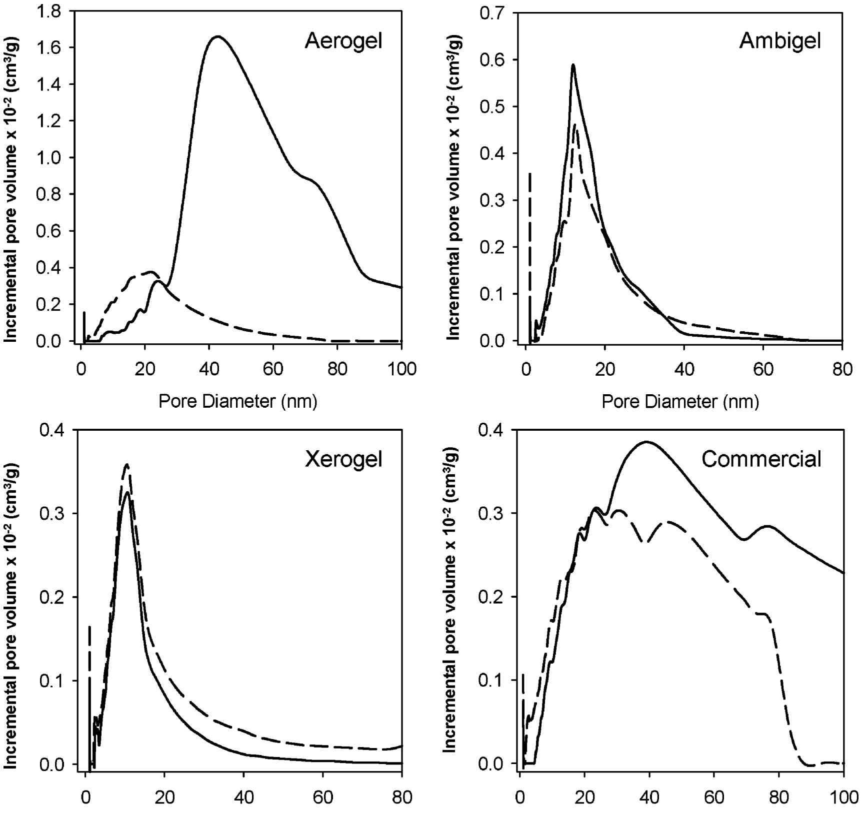

Figure 7. Pore-size distribution plots derived from N_2-adsorption isotherms of 600 °C-calcined powder and pelletized forms of different nanoscopic CeO_2: (—) powder; (- - -) pelletized powder.

Prior to the impedance measurements, the pellets were characterized to determine the effect of the pressing process on their respective pore structures (see Table 1 and Figure 7). The pore structure of the aerogel sample was dramatically altered as it lost 72% of its pore volume. For the other architectures, there was little difference in the pore structures between the powder and pelletized forms. This result is expected for the xerogel and ambigel forms, where the larger

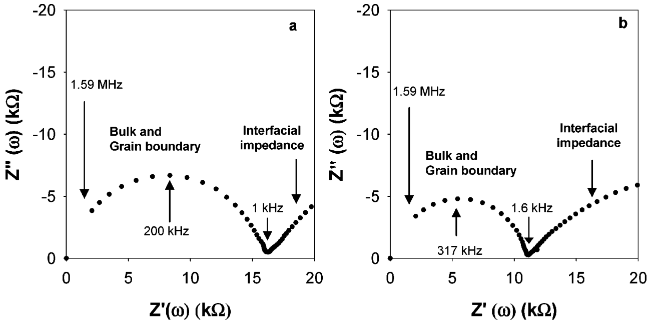

Figure 8. Complex impedance spectrum of nanocrystalline CeO_2 ambigel at 600 °C in (a) O_2 and (b) Ar. Note that the contributions from the bulk and the grain boundaries cannot be distinguished in the high-frequency arc.

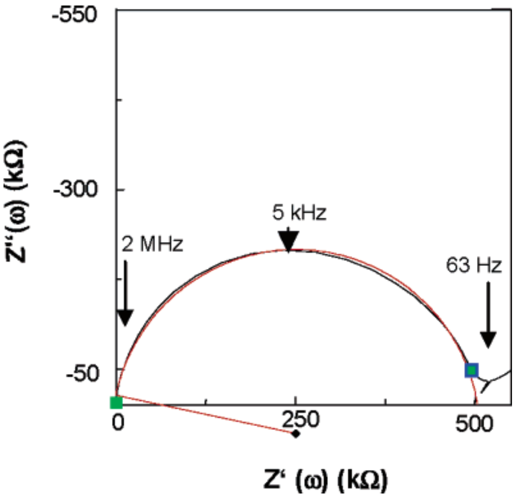

Figure 9. Complex impedance spectrum of nanocrystalline CeO_2 ambigel at 400 °C in O_2. Experimental result in black and simulated result (R||C) in red. Note that the contributions from the bulk and the grain boundaries cannot be distinguished in the high-frequency arc.

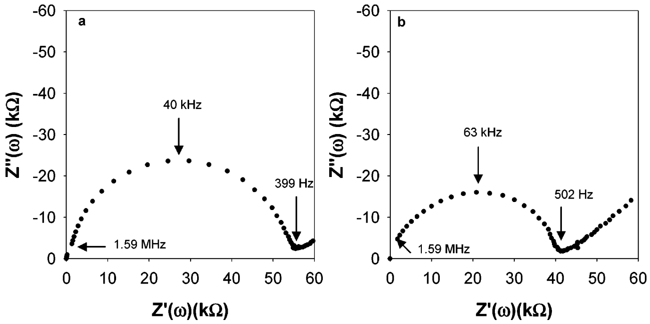

Figure 10. Complex impedance spectra of nanocrystalline CeO_2-commercial at 600 °C in (a) O_2 and (b) Ar. Note that the contributions from the bulk and the grain boundaries cannot be distinguished in the high-frequency arc.

pores present in the initial wet gel (and subsequently retained in the aerogel) have already collapsed due to the capillary forces that develop during ambient-pressure drying.

The electrical behavior of the CeO_2 pellets was examined under pure O_2 and Ar flow over the temperature range 300−600 °C. Representative impedance spectra obtained at 600 °C are presented in Figures 8 and 10. The high-frequency (>1 kHz) impedance response for both CeO_2 ambigel and commercial can be fitted by a single semicircle with a slightly depressed center (Figure 9). An additional low-frequency feature (<1 kHz) is also observed for both samples and with either Pt or Au contacts. This feature is attributed to interfacial effects at the contacting electrodes, as its shape depends on the temperature and atmosphere.

The impedance behavior for nanocrystalline ceria has been previously modeled by an equivalent circuit with two parallel RC elements connected in series, representing bulk and grain boundary responses, respectively.[36−38] According to the reports from the groups of Maier[39] and Tuller[40−42] in which they contrasted the impedance of microcrystalline vs nanocrystalline ceria (>95% dense), the higher frequency "bulk" response is a convolution of conduction in the bulk with a parallel contribution of conduction along grain boundaries. The lower frequency arc was assigned to blocking by grain boundaries perpendicular to current flow. As the particle size is reduced to the nanometer regime, the distinction between bulk and grain boundary regions tends to diminish and the bulk contribution to the impedance response becomes more dominant.[39] However, these previous reports showed that the blocking grain-boundary component is still present even for nanocrystalline ceria and often results in distorted arcs in the impedance spectra.

For both the ambigel and commercial ceria samples that we have evaluated from 300 to 600 °C and under either O_2 or Ar, the resulting impedance spectra can be reasonably modeled with a single semicircle (see Figure 9), indicating that one process dominates the impedance response. This process has a capacitance of ~5×10^{-11} F. For the frequency range over which this semicircle is valid (2 MHz to 1 kHz) and in agreement with the interpretation of Chiang et al.[44] and Tschöpe et al.,[45] we assign this feature to a bulk conduction process. Our 85% dense nanocrystalline materials exhibit minimal contribution to the electrical response from blocking grain boundaries.

The activation energy for ambigel and commercial CeO_2 in the low-temperature region ($T < 600$ °C) was calculated from the Arrhenius plots of the conductivity and was found to be 0.60−0.70 eV for both samples, for either an oxygen or an argon atmosphere. This activation energy is much lower than that reported for single-crystalline CeO_2 (1.97 eV)[43] and coarse-grained ceria (2.45 eV),[44] but comparable to the low activation energy of 0.7 eV already observed in 1-D porous nanocrystalline CeO_2.[43] This result confirms that the conduction mechanism in nanocrystalline and microcrystalline samples differs and reflects the presence of efficient transport pathways in nanocrystalline samples, as previously proposed.[39,40,43] The difference between microcrystalline and

---

(36) Kim, S.; Maier, J. *J. Eur. Ceram. Soc.* **2004**, *24*, 1919−1923.
(37) Chiang, Y.-M.; Lavik, E. B.; Kosacki, I.; Tuller, H. L.; Ying, J. Y. *J. Electroceram.* **1997**, *1*, 7−14.
(38) Tschöpe, A.; Ying, J. Y.; Tuller, H. L. *Sens. Actuators B* **1996**, *31*, 111−114.
(39) Maier, J. *Solid State Ionics* **2002**, *148*, 367−374.
(40) Tuller, H. L. *Solid State Ionics* **1997**, *94*, 63−74.
(41) Tuller, H. L. *Solid State Ionics* **2000**, *131*, 143−157.
(42) Knauth, P.; Tuller, H. L. *Solid State Ionics* **2000**, *136−137*, 1215−1224.
(43) Chiang, Y.-M.; Lavik, E. B.; Kosacki, I.; Tuller, H. L.; Ying, J. Y. *J. Electroceram.* **1997**, *1*, 7−14.
(44) Tschöpe, A.; Sommer, E.; Birringer, R. *Solid State Ionics* **2001**, *139*, 255−266.
(45) Rhodes, C. P.; Dong, W.; Long, J. W.; Rolison, D. R. In *Solid-State Ionics III*; Wachsman, E. D., Swider-Lyons, K. E., Carolan, M. F., Garzon, F. H., Liu, M., Stetter, J. R., Eds.; PV2002-26, Electrochemical Society: Pennington, NJ, 2003; pp 478−489.

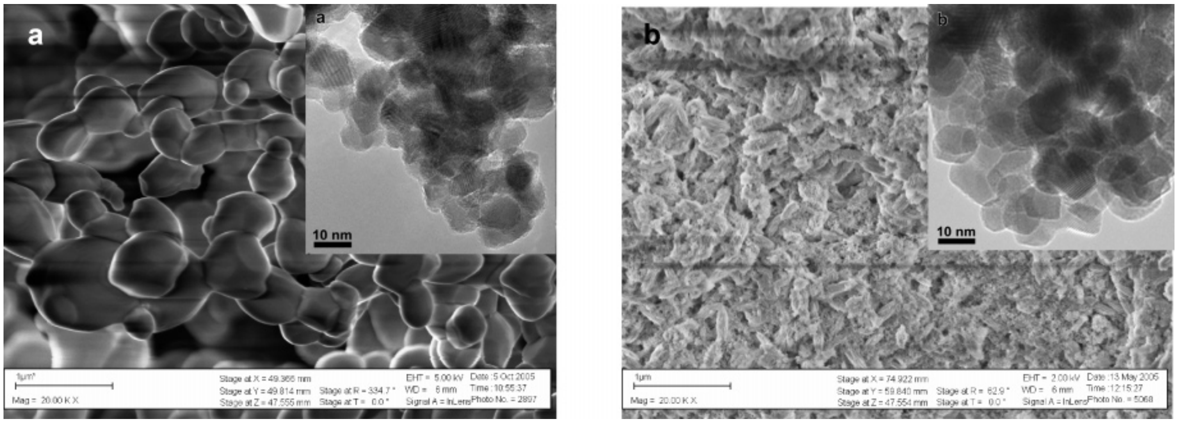

Figure 11. Scanning electron micrographs of 600 °C-calcined nanocrystalline CeO_2 powders: (a) commercial and (b) ambigel. (Insert: Transmission electron micrograph of the studied samples.)

nanocrystalline ceria may be due to the high density of grain boundaries in nanocrystalline ceria that provide preferred paths for transport and extend the interfacial area of the nanocrystalline sample.

Further differences in the electrical response arise if the nanocrystalline oxide is networked rather than agglomerated. The CeO_2 ambigel exhibits higher conductivity than the commercial CeO_2. The conductivity in porous ceramics is a function of such physical attributes as porosity, grain size, and interparticle neck size. The smaller the grain size, the higher the net conductivity, with the grain-size dependence interpreted in terms of positive space-charge model.[40] Most of the studies to date have been performed on dense ceramics. In the space-charge model, a grain boundary consists of a grain boundary core corresponding to a crystallographic mismatch region accompanied by two adjacent space-charge layers. Defects are mostly located in this boundary region. In ultraporous samples, the defect density should not be limited to the grain-boundary interface but may also extend to the entire amplified surface area. Accordingly, defects may include surface adatoms, surface vacancies, and adsorbed species from the contacting atmosphere. Additionally, in nanocrystalline materials, a larger fraction of the solid phase is occupied by the space-charge layer, which should increase the defect concentration and further enhance charge transport. Another factor that may affect the transport properties is the nature and degree of connectivity of interparticle necks. If the contact between the particles is poor, large resistance may be observed.

According to the physical characterizations (Table 1), the two pelletized ceria specimens (ambigel and commercial) are quite similar in terms of the fraction of void volume, primary crystallite size, and specific surface area. The major distinction between these forms of nanoscopic ceria appears to be the microstructure of the solid network (Figure 11). The commercial ceria presents non-networked, agglomerated polydisperse nanocrystallites (scanning and transmission electron micrographs shown in Figure 11a), whereas the ambigels comprise a network of well-defined particles uniformly distributed within the 3-D porous network (Figure 11b). The lower resistivity of the ambigel ceria relative to the commercial sample may, thus, correlate to the more extended and better interconnected transport pathway inherent to the ambigel architecture. Additional studies are ongoing in order to confirm this hypothesis.

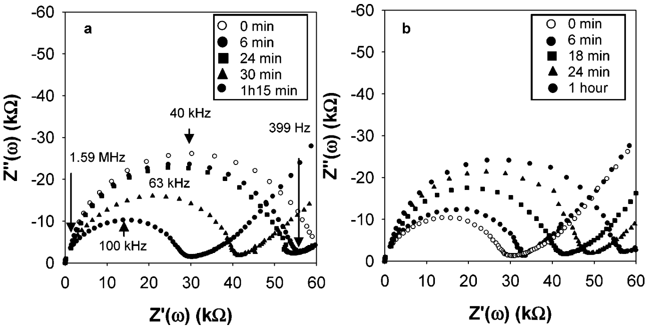

Figure 12. Complex impedance spectrum at 600 °C as a function of time for nanocrystalline CeO_2-commercial in (a) Ar and (b) O_2.

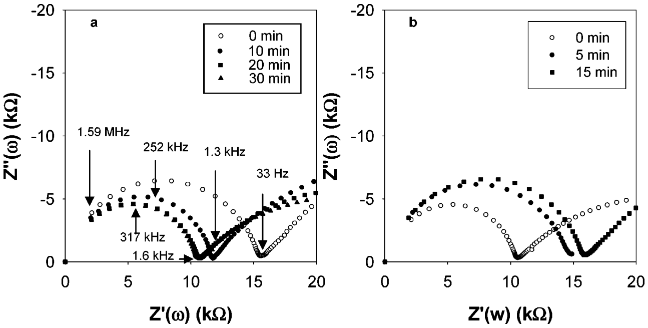

Figure 13. Complex impedance spectrum at 600 °C as a function of time for nanocrystalline CeO_2-ambigel in (a) Ar and (b) O_2.

Further evidence for the conjecture above can be obtained by monitoring the atmospheric effect at 600 °C on the impedance spectra by switching between O_2 and Ar; the results are reported in Figures 12 and 13. In the Ar atmosphere, the resistance of the ambigel and the commercial ceria decreases by ∼30% and 50%, respectively, which is expected due to a lower enthalpy of oxygen vacancy formation at a low partial pressure of oxygen. This result is in agreement with Tschöpe et al., who reported a lower resistivity for nanocrystalline CeO_2 in a reducing atmosphere.[45] However, the resistivity in porous CeO_2 is 75% lower than that of the commercial CeO_2, even though they exhibit comparable surface area and void volume (Table 1). Because the decrease in particle size reduces the enthalpy of defect formation, which should comparably affect both nanocrystalline ceria samples, this difference cannot only be interpreted as grain-size dependence. We attribute the lower resistivity of the ambigel ceria to enhanced O_2 dissociation at its well-defined edges and steps plus a facile transport path along the networked, bonded nanoparticles in the nanoarchitecture.

We investigated the nonstoichiometry of nanocrystalline CeO_2 by thermogravimetry because an increased level of nonstoichiometry increases the concentration of oxygen-ion vacancies, leading to lower resistivity. Isotherms at 600 °C of the ambigel and the commercial nanocrystalline ceria under argon are comparable, although the commercial material exhibits less apparent oxygen deficiency, even though it has slightly higher surface area than the ambigel (45 vs 52 m^2 g^{-1} for the commercial material). Nonstoichiometry, therefore, is playing only a small role in the improved electrical properties of ambigel ceria.

After the samples were heated overnight in pure oxygen, the gas carrier was switched to argon and the impedance spectra were recorded as a function of time (Figures 12a and 13a). The same series of experiments was also performed by heating the sample overnight in argon and switching the gas carrier to pure oxygen (Figures 12b and 13b). Here, again, the impedance spectra of the ambigel and commercial ceria differ. The resistivity of the ambigel pellets is lower than that of the commercial ones. This difference may again arise from the covalently bonded particle contacts in the network, as well as the nature of grain boundary regions and subsurface in the ambigel nanoarchitecture. In addition, the spectral response time is faster for CeO_2-ambigel than CeO_2-commercial. As the activation energies are the same, the mechanism for charge transport in these two nanocrystalline materials must be similar. We, thus, correlate the differences in electrical response to the 3-D nanoarchitecture of the ambigel. Physicochemical characteristics of the nanoarchitecture that plausibly affect the electrical properties include the ease at which oxide nanoarchitectures accommodate defects,[10,45] including a high concentration of surface defects, and shorter solid-state transport distances, providing physically different transport pathways. According to Porat et al.,[46] oxygen losses upon reduction in nanocrystalline ceria are largely due to oxygen desorption from the nanoparticle surfaces. The densities of defects at both surface and interface may then play an important role in this nanoarchitecture.

Conclusions

We have produced nanocrystalline ceria oxide nanoarchitectures that retain the significant porosity and surface area characteristic of the bicontinuous pore−solid networks of aerogels and ambigels. The electrical transport in these nanoarchitectures shows appealing behavior, related to their open, through-connected networks of void volume. The ceria oxidation state and related vacancy of these oxides can be tuned within a certain range to have beneficial electronic conduction in these nanoarchitectures. Further, the degree of mixed conduction in these nanoarchitectures can be controlled. Since such properties as reaction rates and electrical conductivity as well as applications based on these properties (e.g., electrodes, electrolytes, and sensors) are controlled on the basis of the degree of mixed conduction in the oxides, a further exploration of these nanoarchitectures is essential. We are currently exploring new combinations and compositions of pore−solid architectures with the goal of achieving electrode structures that exhibit stability, high ionic conduction, and sufficient electronic conductivity when used as interlayers in solid-oxide fuel cells.

Acknowledgment. Financial support for this work was provided by the U.S. Defense Advanced Research Projects Agency and the U.S. Office of Naval Research. E.M.L. (2000−2003) and M.S.D. (2002−2005) were NRL-NRC postdoctoral associates.

Supporting Information Available: Additional X-ray diffraction data, including figures, text, and a table. This material is available free of charge via the Internet at http://pubs.acs.org.

CM051385T

---

(46) Porat, O.; Lavik, E. B.; Tuller, H. L.; Chiang, Y.-M. In *Nanophase and Nanocomposite Materials, Vol II*; Komarneni, S., Parker, J., Wollenberger, H., Eds.; Materials Research Society: Pittsburgh, PA, 1997; p 99.